PAPER

Check for updates

Curvature-switched activity of carbon nanotube-supported single atom catalysts for the hydrogen evolution reaction†

Wenshan Zhao, Shenyu Shen, YiRu Zhao, Tiantian Wu, [iD] * Shujiang Ding [iD] and Yaqiong Su [iD] *

The hydrogen evolution reaction (HER) is an essential process for hydrogen production through water splitting. Atom-doped carbon nanotubes (CNTs) exhibit significant potential in promoting the electrocatalytic HER. By performing density functional theory (DFT) calculations, we have screened HER performance over a series of single atom transition metals (TM = Mo, Rh, Fe, Cr, Co, Zn, Mn, Cu, Ni, Pd) anchored on CNTs (n, n) $(n = 5, 10)$ and graphene (seen as a CNT with the smallest curvature), and found the volcano curves between the adsorption free energy of H* (ΔG_{H*}) and the current density for the HER, yielding the RhN_4 catalyst at the peak of the volcano and even with a current density higher than that of Pt when the curvature is smaller than (10, 10). Then, more detailed DFT calculations were conducted to investigate the effect of curvature of CNTs on tuning the HER activity of $RhN_4@CNT$ (n, n) $(n = 5–10)$ catalysts, where ΔG_{H*} decreased with the decrease of the curvature, suggesting CNT-supported single atom catalysts having curvature-switched HER activity. The improved HER activity at a higher curvature arose from the more upshifted d-band center. Creating one single vacancy (5-1DB defect) could further enhance the HER activity of $RhN_4@CNTs$. Our work provides a novel approach to designing HER catalysts with tunable activity and stability.

1. Introduction

The depletion of traditional fossil fuels and the environmental pressure are driving the rapid advancement of sustainable energy. As a clean energy, hydrogen energy has attracted increasing attention during the global energy transition.[1,2] Water electrolysis is an effective and feasible method for hydrogen (H_2) generation, in which the hydrogen evolution reaction (HER) is a crucial step.[3] It is well-known that platinum (Pt) is the most common catalyst used due to its excellent catalytic activity and stability during the HER,[4] while the high price of Pt seriously limits its application.[5–8] Thus, the pursuit of novel cost-effective catalysts stands as a paramount objective in the progression of the HER.

Transition metals (TMs), anchored on graphene or carbon nanotubes (CNTs), have attracted much attention due to their flexible structural plasticity, strong stability and unique electronic properties.[9,10] Various single atom TMs based on nitrogen-doped graphene for the HER have been reported both experimentally

and theoretically.[11–15] Despite the notable advantages exhibited by graphene-supported single-atom catalysts, there remains room for improvement in the precise adjustment of catalytic activity. CNTs possess a distinctive three-dimensional structure, enabling facile adjustment of the electronic properties of TMs by manipulating the curvature to achieve higher catalytic activity or selectivity.[16–18] Sun *et al.*[19] have reported the curvature-dependent selectivity in CO_2 reduction on cobalt-porphyrin nanotubes (CoPorNTs), revealing that the Carbon Reduction Reaction (CRR) tends to produce CO at lower-bent nanotubes and CH_4 at higher-bent ones. Cao *et al.*[20] have achieved outstanding HER catalytic activity by modulating the d-band center of $Co_4N@CoSA/N-CNT/CC$, which was regulated effectively by the confined Co_4N nanoparticles in the N-CNTs. Hence, changing the curvature is a potential approach to adjusting the d-band center of the single atom TM doped on graphene/CNTs.

Moreover, carbon nanotubes inherently possess imperfections during their formation. Various defects, including Stone–Wales defects and single vacancy, can be induced or manifest as native defects inevitably.[21–24] These defects may influence the physical and chemical properties of catalysts featuring metals on carbon nanotubes. Ajayan *et al.*[22] have suggested a stable single vacancy defect in CNTs (n, n), formatted by the recombination of three dangling bonds (DBs). The optimal point vacancy defect on CNTs reorganized into a pentagon and a dangling bond, referred to as the 5-1DB defect. Sun *et al.*[25]

School of Chemistry, Engineering Research Center of Energy Storage Materials and Devices of Ministry of Education, National Innovation Platform (Center) for Industry-Education Integration of Energy Storage Technology, Xi'an Jiaotong University, Xi'an 710049, China. E-mail: tianwu@xjtu.edu.cn; yqsu1989@xjtu.edu.cn
† Electronic supplementary information (ESI) available. See DOI: https://doi.org/10.1039/d4ta01719f

have reported tunable defective and carbonylated plasma-treated CNTs (E-CNTs), indicating that the defective carbons on CNTs exhibited the largest contribution rates of the nucleophilic reaction. Evidently, the structure and defects of CNTs are the main factors affecting the catalytic activity. However, the effect of defects on the catalytic HER performance of CNT-supported single atom TMs remains unclear.

Herein, we employed density functional theory (DFT) calculations to thoroughly screen a range of TMs (TM = Mo, Rh, Fe, Cr, Co, Zn, Mn, Cu, Ni, Pd) anchored on graphene and CNTs for HER catalytic activity and found that TMs loaded on graphene perform better for hydrogen adsorption compared to those on CNT substrates. It was also observed that the carbon-based RhN_4 site shows the highest HER activity. Then we systematically investigated the curvature effect on the catalytic performance of $RhN_4@CNTs$ (n, n) $(n = 5$–$10)$ in the HER. Finally, we explored the influence of 5-1DB defects of CNTs on the HER activity. Our work provides a profound comprehension of the curvature effect on the HER catalyzed by $RhN_4@CNTs$, and proposes a rational material design scheme for CNT-supported catalysts with tuneable activity in experimental endeavors.

2. Computational methods

All the calculations are carried out by using density functional theory (DFT) methods implemented in the Vienna *Ab Initio* Simulation Package (VASP)[26,27] with the revised Perdew–Burke–Ernzerhof (PBE) functional[28] based on the generalized-gradient approximation. A plane-wave basis was set with a cut-off energy of 400 eV.[29,30] For the structural optimizations of $TMN_4@C$, the Monkhorst–Pack k-point mesh of $3 \times 3 \times 1$ is used for the Brillouin zone integration. And for $TMN_4@CNTs$, the k-point grid is $1 \times 1 \times 5$. The effect of core–valence interactions is described by the projector augmented wave (PAW) method.[30] The energy and force convergence criteria were set to 10^{-4} eV per atom and -0.05 eV $Å^{-1}$, respectively. Vibrational frequencies are calculated over the Γ point to obtain zero-point energies (ZPEs), thermal corrections, and entropy contributions.

CNTs (n, n) $(n = 5$–$10)$ with different curvatures were constructed as the basis to build $RhN_4@CNT$ (n, n) $(n = 5$–$10)$ and de-$RhN_4@CNT$ (n, n) $(n = 5$–$10)$ structures.

The adsorption energy (ΔE_{H*}) of hydrogen on $RhN_4@CNTs$ was calculated by using the equation

$$\Delta E_{H*} = E_{cat+H} - E_{cat} - 1/2E_{H_2}$$

where E_{cat+H} and E_{cat} are the calculated energies of the CNTs with and without the adsorbed hydrogen atom. E_{H_2} represents the energy of the H_2 molecule in the gas phase.

The catalytic activity of the HER can be evaluated using ΔG_{H*}, which can describe the adsorption strength of H on the catalysts.

$$\Delta G_{H*} = \Delta E_{H*} + \Delta E_{ZPE} \pm T\Delta S_H + \Delta G_{pH}$$

where ΔE_{ZPE} is the zero-point energy difference between the adsorbed state and free gas H_2 molecule. ΔS_H is the entropy

between the adsorbed H and half of H_2 molecule in the gas phase. The zero-point energy and entropy are calculated under the standard conditions corresponding to the pressure of 101 325 Pa ($\sim$1 bar) of H_2 at the temperature of 298.15 K. ΔG_{pH} is the correction of the H^+ free energy by the concentration, which can be evaluated as $\Delta G_{pH} = 2.303 \times k_BT \times pH$ eV, here the value of pH was assumed to be zero.

To predict HER activity, the theoretical exchange current density (i_0)[31] was calculated by using the equation

$$i_0 = -ek_0 \frac{1}{1 + \exp(-\Delta G_{H*}/k_BT)}, \quad \Delta G_{H*} \leq 0$$

$$i_0 = -ek_0 \frac{1}{1 + \exp(\Delta G_{H*}/k_BT)}, \quad \Delta G_{H*} > 0$$

where k_0 is set to 200 s^{-1} per site and taken from ref. 31. k_B is the Boltzmann constant and T is set to 298.15 K.

3. Results and discussion

3.1 Screening of HER catalytic performance on $TMN_4@C$/CNTs

Generally, the Gibbs free energy ΔG_{H*} is considered to be an appropriate descriptor of HER reactivity, which shows the adsorption strength of H atom on the catalyst.[33] It is worth noting that strong adsorption does not imply high catalytic activity. Adsorption that is too strong will make it difficult to desorb the product, while too weak adsorption indicates the challenge of H adsorption at the catalytic site. For the HER, superior catalytic activity can be achieved when ΔG_{H*} is close to 0 eV.[34–36] This condition facilitates a rapid proton/electron-transfer step and an expedited hydrogen desorption process.[36] Graphene can be approximated as carbon nanotubes with an extremely low curvature. Therefore, a 4×4 graphene model was selected to load TM atoms, together with the CNTs (n, n) $(n = 5, 10)$, screening for high-performance single-atom catalysts. As shown in Fig. 1a, the Gibbs free energies of H adsorption on $TMN_4@C$ and $TMN_4@CNTs$ (n, n) $(n = 5, 10)$ (TM = Mo, Rh, Fe, Cr, Co, Zn, Mn, Cu, Ni, Pd) were calculated. The computational results demonstrated that graphene-based single atom catalysts exhibit a stronger hydrogen adsorption capability than those on CNTs, while TMs on CNTs (10, 10) with less curvature show lower ΔG_{H*} than those on CNTs (5, 5). Thus, DFT calculations suggest that reducing the curvature of CNTs can enhance the adsorption of H atom on catalysts. Moreover, the HER catalytic performance of Rh metal is most outstanding. The configurations of H adsorption and relaxed binding energies (E_b) are shown in Fig. S1 and S2 and Tables S1 and S2 of the ESI.† The volcano curves between the adsorption free energy of H* (ΔG_{H*}) and the current density for the HER were found, yielding the $RhN_4@CNTs$ (10, 10) and $RhN_4@C$ catalysts at the peak of the volcano with a current density higher than Pt, as shown in Fig. 1c and d. Metals at the top of the volcano perform well with an optimal H-binding energy. Thus, the results revealed that Rh metal anchored on both graphene and CNTs has adequate ΔG_{H*} and high exchange current density (i_0) to adsorb and desorb H

This journal is © The Royal Society of Chemistry 2024

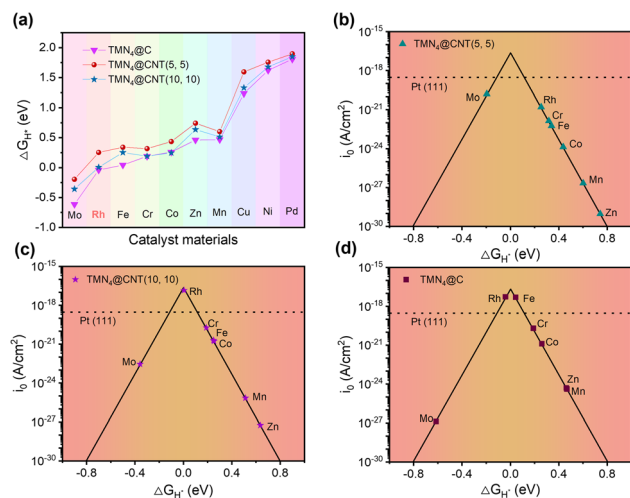*J. Mater. Chem. A*, 2024, **12**, 16476–16481 | **16477**

Fig. 1 DFT-calculated Gibbs free energies and volcano plots of the exchange current density. (a) Gibbs free energy of H adsorption (ΔG_{H*}) on TMN$_4$@C and TMN$_4$@CNTs (n, n) (n = 5, 10), TM = Mo, Ru, Rh, Fe, Cr, Co, Ag, Zn, Mn, Cu, Ni, Pd. (b)–(d) Volcano plot between exchange current density (i_0) and ΔG_{H*} in TMN$_4$@CNTs (n, n) (n = 5, 10) and TMN$_4$@C. Data for the Pt (111) surface were obtained from ref. 32.

atom, which was screened out to further construct the single-atom catalyst on CNTs with different curvatures.

In addition to the high HER activity, the RhN$_4$ catalyst has been found to have high thermodynamic stability, which is analysed by investigating the binding energy (E_b) and the cohesive energy (E_{coh}) of Rh via the following formulae:

$$E_b = E_{total} - E_{Rh} - E_{sub}$$

$$E_{coh} = E_{Rh\text{-}bulk/n} - E_{Rh\text{-}single}$$

where E_{total}, E_{sub} and E_{Rh} represent the energies of catalyst structures, Rh-free based structure, and Rh atom, respectively. As noted in Fig. 2, the single-atom structure of Rh is thermodynamically stable on both graphene and CNTs with different curvatures.
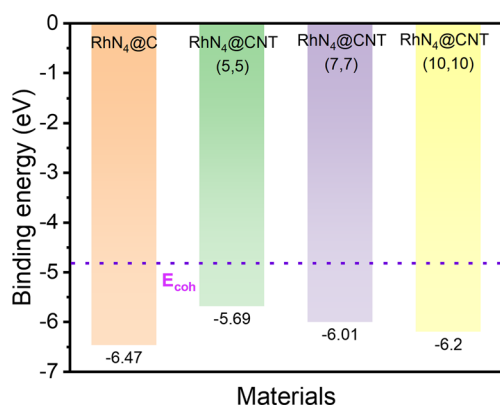

Fig. 2 The calculated cohesive energy of Rh and the binding energy (E_b) of RhN$_4$@C and RhN$_4$@CNTs (n, n) (n = 5, 7, 10).

3.2 HER catalytic activity of RhN$_4$@CNTs (n, n) (n = 5–10)

The Rh metal single-atom catalyst exhibited appropriate interactions with H, showcasing the potential for efficient catalysis of the HER while maintaining thermodynamic stability. Thus, the geometric models of RhN$_4$@CNTs with different nanotube diameters were constructed to study the effect of curvature on the HER performance (Fig. 3a). The optimized structural parameters and associated key structural parameters are shown in Fig. S3 and Table S3.† As shown in Fig. 3b, ΔG_{H*} declined and approached nearly zero when n = 10, which illustrated that a decrease in carbon nanotube curvature is conducive to enhanced hydrogen adsorption on the catalytic surface.

As a valid descriptor for the HER, the d-band center was also calculated to analyze the adsorption properties of catalytic materials. The position of the d-band center influences the activity of the catalytic reaction. The distance between the d-band center and Fermi level can predict the performance of catalysts during the processes of adsorption and dissociation in the HER. The proximity of the d-band center to the Fermi level facilitates more efficient electron transfer, thereby enhancing the adsorption strength of the adsorbate and improving the catalytic activity.[37] As shown in Fig. 3c, it is found that the d-band centers have a correlation with ΔG_{H*} (R^2 = 0.99), indicating that the d-band center was a highly effective descriptor for RhN$_4$@CNT catalysts. Crucially, there is also a correlation between the curvature and the position of the d-band center. When n = 10, the d-band center exhibited the smallest value, which was the closest proximity to the Fermi level, resulting in the lowest ΔG_{H*}. The decrease in the curvature led to the tailoring of ε_d, bringing it closer to the Fermi level. As a result, the catalyst exhibited stronger hydrogen adsorption affinity. Therefore, adjusting the curvature can be an approach to set ε_d in a carbon nanotube-based single atom catalyst to regulate the adsorption strength.

The effect of curvature on the catalytic performance was further analyzed by state density, as shown in Fig. 4. The PDOS
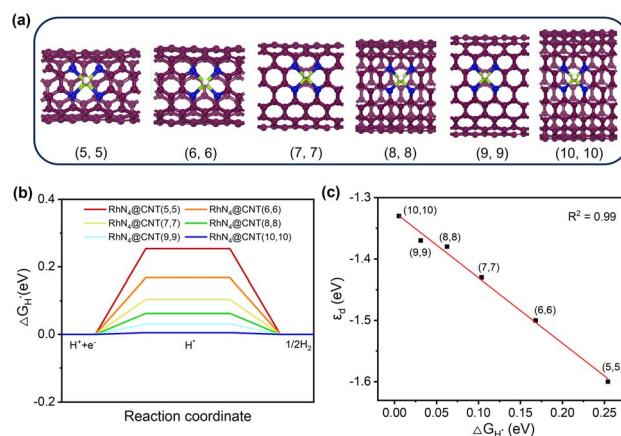

Fig. 3 HER activity of RhN$_4$@CNTs with six different curvatures. (a) Optimized geometric model of RhN$_4$@CNTs (n, n) (n = 5–10) adsorbed with a single H atom. (b) ΔG_{H*} on RhN$_4$@CNTs (n, n) (n = 5–10). (c) Correlation between ΔG_{H*} and d-band center (ε_d) of Rh anchored on CNTs with different nanotube diameters.
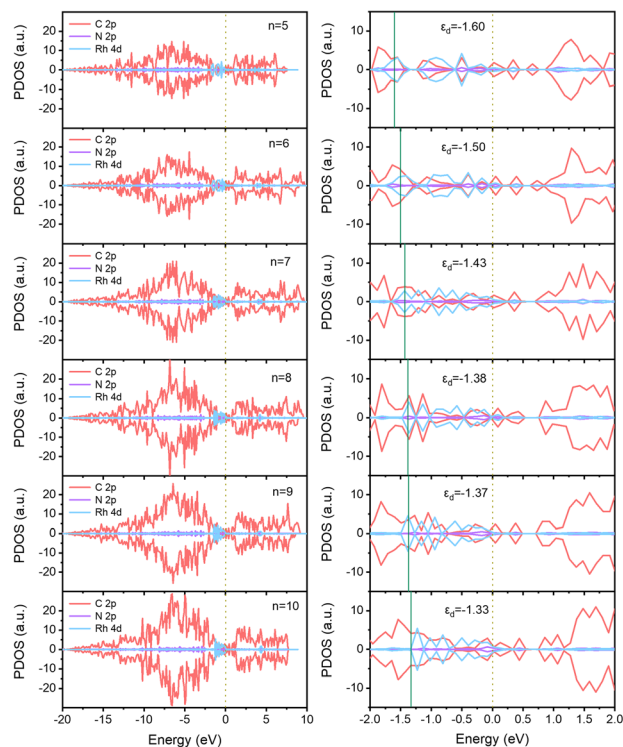
16478 | J. Mater. Chem. A, 2024, **12**, 16476–16481

This journal is © The Royal Society of Chemistry 2024

Fig. 4 Partial density of states (PDOS) for RhN$_4$@CNTs (n, n) (n = 5–10), C-state, N-state, and Rh-state are represented by red, purple, and blue. On the right is an enlarged view in the energy range of −2 to 2 eV. The dotted line and the full line represent the position of the Fermi level and d-band center (ε_d), respectively.

of RhN$_4$@CNTs (n, n) (n = 5–10) revealed a noteworthy involvement of the d orbitals of Rh atom in the DOS at the Fermi level, indicating robust hybridization between the d states of Rh atom and the p states of C and N atoms. With the decreasing of curvature, the DOS of C at 2p states below the Fermi level is expanded, and the 4d states of Rh overlaps more with the 2p states of C, suggesting the enhanced electron interaction among C, N and Rh. The enlarged diagram showed that as the curvature decreased, the d-band center moved closer to the Fermi level, resulting in the enhancement of hydrogen adsorption on RhN$_4$@CNTs. Hence, by modulating the curvature of carbon nanotubes, the control of the material's d-band center can be achieved, subsequently regulating the catalytic reaction activity.

3.3 The 5-1DB defect on RhN$_4$@CNTs

Perfect carbon nanotubes show remarkable performance in the fields of mechanics, thermodynamics and chemistry. However, in the process of generating carbon nanotubes, various structural defects will inevitably be formed such as single vacancy and Stone–Wales defects.[38] In contrast to the common perception, the defects did not negatively affect the performance of the CNTs. Instead, it can improve the chemical properties of CNTs and make new functions possible.[39–41] For armchair carbon nanotubes (n, n), 5-1DB is a common defect resulting from the absence of a single carbon atom.[22] This single point defect leads
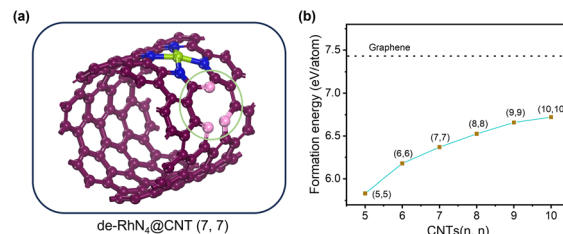

Fig. 5 Defect formation energies as a function of n of CNTs. (a) Optimized structure of de-RhN$_4$@CNTs (7, 7) with a 5-1DB defect. (b) The formation energy of a 5-1DB defect on graphene and RhN$_4$@CNTs (n, n) (n = 5–10).

to the creation of three dangling bonds (DBs) which are unstable. Through the recombination of three DBs, a five-ring structure and a DB are formed, which is called the 5-1DB defect. In order to explore the effect of the defect on RhN$_4$@CNTs during the HER, a 5-1DB defect was created, as shown in Fig. 5. And the formation energy of the defects on CNTs was calculated. Although the defect formation energy for RhN$_4$@CNTs (n, n) (n = 5–10) increased monotonically with decreasing curvature, it remains lower than that on graphene, indicating that creating one 5-1DB defect on CNTs is more facile than on graphene. Therefore, the consideration of the presence of defects on CNTs is indispensable for assessing the impact on catalytic reactions.

3.4 HER catalytic activity of de-RhN$_4$@CNTs (n, n) (n = 5–10)

As shown in Fig. 6a, the geometric models of de-RhN$_4$@CNTs (n, n) (n = 5–10) were constructed, containing a 5-1DB defect neighboring the single atomic site. The Gibbs free energy calculation (Fig. 6b) revealed that ΔG_{H*} decreased as the curvature of the CNTs reduced. Compared to the catalysts without any defect (Fig. 3b), a 5-1DB defect on the CNTs caused a lower ΔG_{H*}. For the HER on RhN$_4$@CNTs, ΔG_{H*} approached zero when n = 10, while for that on de-RhN$_4$@CNTs, ΔG_{H*} was close to zero as n = 7. Thus, the 5-1DB defect greatly reduced the ΔG_{H*} of H adsorption, leading to a stronger interaction between hydrogen and catalysts. The presence of individual 5-1DB defect on CNTs is conducive to promoting the HER. As the curvature decreased, the d-band center upshifted more closer to the Fermi level, and a linear relationship (R^2 = 0.82) existed between ΔG_{H*} and ε_d, as shown in Fig. 6c.

Subsequently, to deeply understand the optimal intrinsic activity of the HER on de-RhN$_4$@CNTs, PDOS and the d-band centers were computed. The PDOS of de-RhN$_4$@CNTs (n, n) (n = 5–10) also revealed strong hybridization between the d states of Rh atom and the p states of C and N atoms (Fig. 7). Strong electron transfer still existed between C atoms, N atoms and Rh atoms. Compared with the perfect carbon nanotubes, the 5-1DB defect changed the local electron density distribution on de-RhN$_4$@CNTs, which affected the shape and position of the electronic state, so that the peak of the 2p states of C was less sharp in the enlarged image on the right of Fig. 7. Given the close association between the d-band center and the electronic structure of transition metals, alterations in the electronic
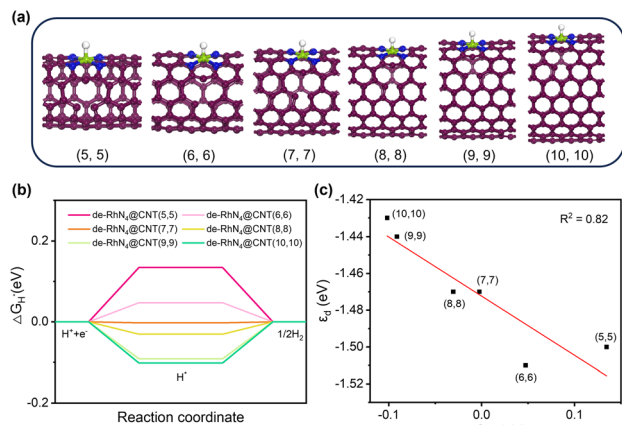
This journal is © The Royal Society of Chemistry 2024

J. Mater. Chem. A, 2024, **12**, 16476–16481 | **16479**

Fig. 6 HER activity of de-RhN$_4$@CNTs with six different curvatures. (a) Optimized geometric model of de-RhN$_4$@CNTs (n, n) (n = 5–10) adsorbed with hydrogen. (b) Calculated Gibbs free energy ΔG_{H*} on de-RhN$_4$@CNTs (n, n) (n = 5–10). (c) Correlation between ΔG_{H*} and d-band center (ε_d).

structure induced by defects may lead to uncertainty in the position of the d-band center. The d-band center of metallic Rh in the de-RhN$_4$@CNTs was similar when n = 5, 6, n = 7, 8, n = 9, 10, respectively. From the overall trend in the data of ε_d, it was still observed that the d-band center moved closer to the Fermi level with a decrease in curvature.
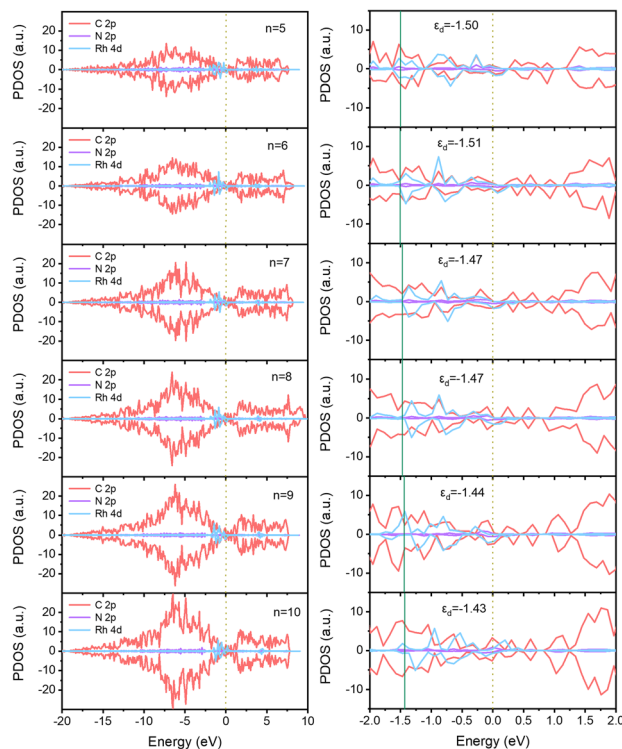

Fig. 7 PDOS for de-RhN$_4$@CNTs (n, n) (n = 5–10), C-state, N-state, and Rh-state are represented by red, purple, and blue. The right is an enlarged view in the energy range of −2 to 2 eV. The dotted line and the full line represent the position of the Fermi level and d-band center (ε_d), respectively.
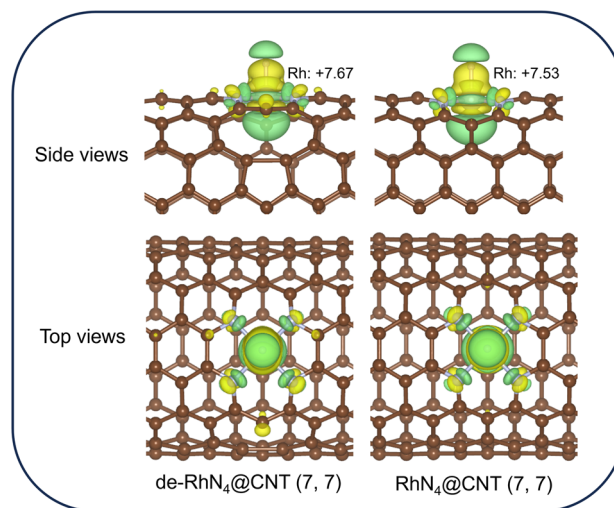

Fig. 8 Bader charge, and charge density difference for H atom adsorption on RhN$_4$@CNTs (7, 7) and de-RhN$_4$@CNTs (7, 7). The yellow region represents charge accumulation, and the cyan region represents charge depletion. The isosurface value is 0.002 e bohr^{-3}.

The 5-1DB defect introduced local curvature and distortion, resulting in changes of the local electronic structure of carbon nanotubes. To analyze the change of electron distribution in the 5-1DB defect, the charge density difference of RhN$_4$@CNTs (7, 7) and de-RhN$_4$@CNTs (7, 7) with H atom adsorption were calculated (Fig. 8). The 5-1DB defect enriched the charge density on the nearby C atoms, increasing the charge density of the adsorption site region. Furthermore, the charge density of Rh atoms also increased, which enhanced the interaction between Rh metal and the H atom, directly. Bader charge showed that the atomic charges of Rh in de-RhN$_4$@CNTs (7, 7) (+7.67e) are more positive than those in RhN$_4$@CNTs (7, 7) (+7.53e). Therefore, the 5-1DB defect facilitated the adsorption of hydrogen on de-RhN$_4$@CNTs.

4. Conclusions

In this work, we have performed computational screening of a series of TMs (TM = Mo, Rh, Fe, Cr, Co, Zn, Mn, Cu, Ni, Pd) anchored on graphene and CNTs for catalyzing the HER, with Rh showcasing the best HER activity. Then, we explored the effects of curvature and 5-1DB defect on the HER catalytic activity of the RhN$_4$@CNTs (n, n) (n = 5–10). Our results indicate a linear relationship between the d-band center and curvature of CNTs, so that the H adsorption of RhN$_4$@CNTs can be regulated precisely by altering the curvature. The interaction of Rh metal with H atom increases as the curvature of the carbon nanotubes decreases. The 5-1DB defect affects the local electronic structure near the active site, which is conducive to tuning the binding between Rh metal and H atom and further regulating HER activity. The improved HER activity is explained by the upshift of the d-band center. Thus, the adjustment of curvature or the formation of the 5-1DB defect can regulate the binding energy of H atom on RhN$_4$@CNTs and further affects the catalytic activity. Our findings shed light on

16480 | *J. Mater. Chem. A*, 2024, **12**, 16476–16481

This journal is © The Royal Society of Chemistry 2024

the design of efficient carbon nanotube-supported catalysts and contribute to the innovative advancements in catalyst development.

Conflicts of interest

There are no conflicts to declare.

Acknowledgements

References

1 J. A. Turner, *Science*, 2004, **305**, 972–974.

2 Y. Yan, L. Thia, B. Y. Xia, X. Ge, Z. Liu, A. Fisher and X. Wang, *Adv. Sci.*, 2015, **2**, 1500120.

3 J. K. Norskov and C. H. Christensen, *Science*, 2006, **312**, 1322–1323.

4 S. Bai, C. Wang, M. Deng, M. Gong, Y. Bai, J. Jiang and Y. Xiong, *Angew. Chem., Int. Ed. Engl.*, 2014, **53**, 12120–12124.

5 S. Sultan, J. N. Tiwari, A. N. Singh, S. Zhumagali, M. Ha, C. W. Myung, P. Thangavel and K. S. Kim, *Adv. Energy Mater.*, 2019, **9**, 1900624.

6 Z. W. Seh, J. Kibsgaard, C. F. Dickens, I. Chorkendorff, J. K. Nørskov and T. F. Jaramillo, *Science*, 2017, **355**, eaad4998.

7 A. Bharti and G. Cheruvally, *J. Power Sources*, 2017, **360**, 196–205.

8 H. Yin, S. Zhao, K. Zhao, A. Muqsit, H. Tang, L. Chang, H. Zhao, Y. Gao and Z. Tang, *Nat. Commun.*, 2015, **6**, 6430.

9 X. Zhang, A. Chen, Z. Zhang, M. Jiao and Z. Zhou, *J. Mater. Chem. A*, 2018, **6**, 11446–11452.

10 Y. Li, D. Bahamon, M. Sinnokrot and L. F. Vega, *npj Comput. Mater.*, 2022, **8**, 229.

11 Z. Chen, H. Qing, R. Wang and R. Wu, *Energy Environ. Sci.*, 2021, **14**, 3160–3173.

12 H. Cao, Q. Wang, Z. Zhang, H.-M. Yan, H. Zhao, H. B. Yang, B. Liu, J. Li and Y.-G. Wang, *J. Am. Chem. Soc.*, 2023, **145**, 13038–13047.

13 J. Guo, J. Liu, X. Mao, S. Chu, X. Zhang, Z. Luo, J. Li, B. Wang, C. Jia and D. Qian, *J. Phys. Chem. Lett.*, 2022, **13**, 5195–5203.

14 S. Aralekallu, L. K. Sannegowda and V. Singh, *Int. J. Hydrogen Energy*, 2023, **48**, 16569–16592.

15 K. Munoz-Becerra, F. J. Recio, R. Venegas and J. H. Zagal, *Curr. Opin. Electrochem.*, 2023, **42**, 101387.

16 W. Liu, K. Guo, Y. Xie, S. Liu, L. Chen and J. Xu, *Sci. Rep.*, 2023, **13**, 9926.

17 N. Ma, Y. Zhang, Y. Wang, J. Zhao, B. Liang, Y. Xiong, S. Luo, C. Huang and J. Fan, *J. Colloid Interface Sci.*, 2024, **654**, 1458–1468.

18 M. De Volder, S. Park, S. Tawfick and A. J. Hart, *Nat. Commun.*, 2014, **5**, 4512.

19 G. Zhu, Y. Li, H. Zhu, H. Su, S. H. Chan and Q. Sun, *ACS Catal.*, 2016, **6**, 6294–6301.

20 C. Bo, H. Minghao, C. Yan, J. Peng, L. Baocang, Z. Bo, W. Xi, G. Rui, S. Xiaolei, D. Yaping and Z. Jun, *NPG Asia Mater.*, 2021, **13**, 1.

21 R. Jussane, R. Baierle, A. Fazzio and R. Mota, *Nano Lett.*, 2005, **5**, 197–200.

22 P. M. Ajayan, V. Ravikumar and J. C. Charlier, *Phys. Rev. Lett.*, 1998, **81**, 1437–1440.

23 L. G. Zhou and S. Q. Shi, *Appl. Phys. Lett.*, 2003, **83**, 1222–1224.

24 A. V. Krasheninnikov, K. Nordlund, M. Sirviö, E. Salonen and J. Keinonen, *Phys. Rev. B: Condens. Matter Mater. Phys.*, 2001, **63**, 245405.

25 C. Sun, H. Wang, T. Jiang, X. Zhao, M. Yao, X. Wang, Y. Zhu, D. Wang, Z. Li, Y. Hou, L. Lei and B. Yang, *Sep. Purif. Technol.*, 2024, **337**, 126454.

26 G. Kresse and J. Furthmuller, *Phys. Rev. B: Condens. Matter Mater. Phys.*, 1996, **54**, 11169–11186.

27 G. Kresse and J. Furthmuller, *Comput. Mater. Sci.*, 1996, **6**, 15–50.

28 B. Hammer, L. B. Hansen and J. K. Norskov, *Phys. Rev. B: Condens. Matter Mater. Phys.*, 1999, **59**, 7413–7421.

29 P. E. Blochl, *Phys. Rev. B: Condens. Matter Mater. Phys.*, 1994, **50**, 17953–17979.

30 G. Kresse and D. Joubert, *Phys. Rev. B: Condens. Matter Mater. Phys.*, 1999, **59**, 1758–1775.

31 J. K. Norskov, T. Bligaard, A. Logadottir, J. R. Kitchin, J. G. Chen, S. Pandelov and J. K. Norskov, *J. Electrochem. Soc.*, 2005, **152**, J23–J26.

32 T. F. Jaramillo, K. P. Jorgensen, J. Bonde, J. H. Nielsen, S. Horch and I. Chorkendorff, *Science*, 2007, **317**, 100–102.

33 R. Subbaraman, D. Tripkovic, D. Strmcnik, K.-C. Chang, M. Uchimura, A. P. Paulikas, V. Stamenkovic and N. M. Markovic, *Science*, 2011, **334**, 1256–1260.

34 B. Hinnemann, P. G. Moses, J. Bonde, K. P. Jorgensen, J. H. Nielsen, S. Horch, I. Chorkendorff and J. K. Norskov, *J. Am. Chem. Soc.*, 2005, **127**, 5308–5309.

35 F. Li, G.-F. Han, H.-J. Noh, J.-P. Jeon, I. Ahmad, S. Chen, C. Yang, Y. Bu, Z. Fu, Y. Lu and J.-B. Baek, *Nat. Commun.*, 2019, **10**, 4060.

36 Y.-Y. Ma, C.-X. Wu, X.-J. Feng, H.-Q. Tan, L.-K. Yan, Y. Liu, Z.-H. Kang, E.-B. Wang and Y.-G. Li, *Energy Environ. Sci.*, 2017, **10**, 788–798.

37 B. Hammer and J. K. Norskov, *Nature*, 1995, **376**, 238–240.

38 M. Dhawan, R. S. Dondapati and S. Sharma, *International Conference on Computational Science*, 2018, pp. 209–212.

39 K. Sharma, K. K. Saxena and M. Shukla, *Procedia Eng.*, 2012, **38**, 3373–3380.

40 J. Kumar, Ansh and M. Shrivastava, *ACS Omega*, 2020, **5**, 31281–31288.

41 A. V. Stepanov, *J. Surf. Invest.: X-Ray, Synchrotron Neutron Tech.*, 2013, **7**, 218–222.

This journal is © The Royal Society of Chemistry 2024

J. Mater. Chem. A, 2024, **12**, 16476–16481 | **16481**